JVST A
Journal of Vacuum Science & Technology A

ARTICLE

avs.scitation.org/journal/jva

Atomic layer deposition of hafnium and zirconium oxyfluoride thin films

Cite as: J. Vac. Sci. Technol. A 39, 022403 (2021); doi: 10.1116/6.0000731
Submitted: 20 October 2020 · Accepted: 29 December 2020 ·
Published Online: 29 January 2021

Neha Mahuli, Andrew S. Cavanagh, and Steven M. George

AFFILIATIONS

Department of Chemistry, University of Colorado, Boulder, Colorado 80309-0215

Note: This paper is part of the 2021 Special Topic Collection on Atomic Layer Deposition (ALD).

ABSTRACT

Hafnium and zirconium oxyfluoride films may act as effective protective coatings during plasma processing. The low molar volume expansion/contraction ratios and the small estimated strain values versus fluorination/oxidation suggest that hafnium and zirconium oxyfluorides can serve as protective coatings in both fluorine and oxygen plasma environments. To demonstrate the procedures for depositing these films, hafnium and zirconium oxyfluorides with tunable stoichiometry were grown using atomic layer deposition (ALD) at 150 °C. Tetrakis(dimethylamido)hafnium and tetrakis(ethylmethylamido)zirconium were used as the metal precursors. H_2O and HF were employed as the oxygen and fluorine precursors, respectively. MO_xF_y (M = Hf and Zr) films were grown using two deposition mechanisms: the nanolaminate method and the HF exchange method. *In situ* quartz crystal microbalance studies were employed to monitor the MO_xF_y growth. Both deposition methods observed a linear MO_xF_y growth at 150 °C. The nanolaminate method is defined by the sequential deposition of MO_x ALD and MF_y ALD layers. Compositional tunability was achieved by varying the ratio of the number of MO_x ALD cycles to the number of MF_y ALD cycles in the nanolaminate. The HF exchange method is based on the thermodynamically favorable fluorination reaction of MO_x by HF. Variable oxygen-to-fluorine concentrations in these films were obtained either by changing the HF pressure or by varying the thickness of the underlying MO_x ALD layers. *Ex situ* Rutherford backscattering spectroscopy measurements were utilized to determine the composition of the various MO_xF_y thin films. Both deposition techniques displayed a wide range of compositional tunability from HfO_2 to HfF_4 and ZrO_2 to ZrF_4. In addition, the physical sputtering rates of MO_xF_y films were estimated from the film removal rates during *ex situ* x-ray photoelectron spectroscopy depth profiling. The physical sputtering rates increased with F concentration in the MO_xF_y films.

I. INTRODUCTION

Metal oxide and metal fluoride coatings can act as protective coatings against corrosion during plasma processing. Plasma processes utilize various corrosive gases, including CF_4, SF_6, NF_3, Cl_2, and O_2, in semiconductor device fabrication. Protective coating materials are essential to reduce particle generation, device contamination, and erosion of chamber walls and components resulting from plasma exposure.[1–5] Metal oxides, such as Y_2O_3, show lower rates of erosion than their metal fluoride counterparts in oxygen-containing plasmas.[6,7] Y_2O_3 and Al_2O_3 have been successfully established as protective coatings in oxygen-rich plasma environments.[6–9] However, metal oxides also show higher rates of erosion in fluorine-based plasma environments than their metal fluoride counterparts.[6,7,10] As a result, metal fluorides, such as YF_3, have been applied as a protective coating in fluorine-rich plasma environments.[6,10]

Exposure to fluorine or oxygen plasmas can lead to volume expansion or contraction, as illustrated in Fig. 1. Metal oxides (MO_x) in fluorine-containing plasmas undergo fluorination, resulting in volume expansion and compressive stress in the top few layers of the metal fluoride, as shown in Fig. 1(a). Similarly, metal fluorides (MF_y) in oxygen-containing plasmas undergo oxidation, resulting in volume contraction and tensile stress in the top few layers of the metal oxide, as displayed in Fig. 1(b). The stress induced as a result of fluorination or oxidation can cause film cracking and particle generation in these MO_x or MF_y films.[7–9,11]

In contrast, oxyfluoride films should experience less stress when they are exposed to either fluorine- or oxygen-based plasmas. Recently, metal oxyfluorides like YO_xF_y and AlO_xF_y have received attention as possible protective coatings.[7,12–16] The choice of metal cations in these oxyfluorides plays an important role in tuning the

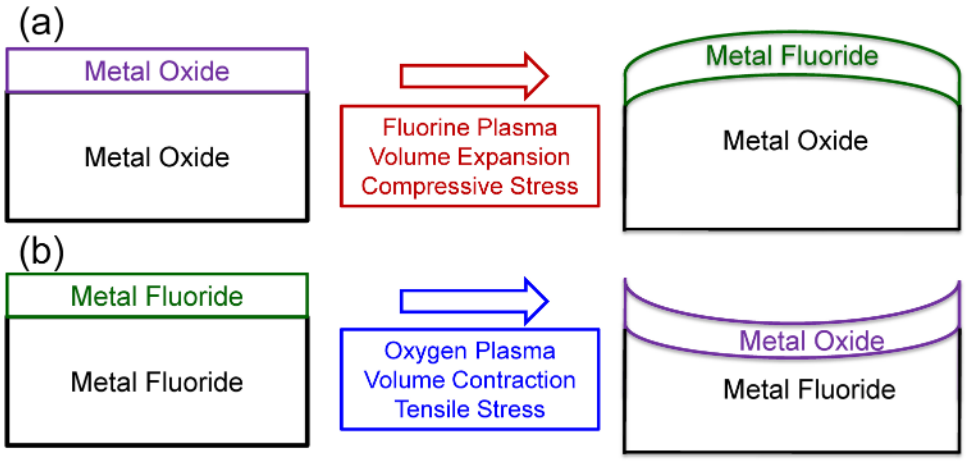

FIG. 1. Schematic of (a) volume expansion during fluorination of metal oxide to metal fluoride by fluorine plasma and (b) volume contraction during the oxidation of metal fluoride to metal oxide by oxygen plasma. Volume expansion and contraction lead to compressive and tensile stress, respectively, in the surface layers.

corrosion resistance properties. Various metal cation systems have been proposed as candidates for protective coatings, including Hf, Zr, Nb, and rare earth elements.[17] The reduction of particle formation in these films relies on minimal change in the molar volume between the metal oxide and the metal fluoride during oxidation or fluorination. This minimal change in the molar volume lowers the film strain upon fluorination or oxidation. Using the ratio of the molar volume of the metal oxide and metal fluoride as a figure of merit, Hf and Zr oxyfluorides show comparable ratios to Y oxyfluorides. As a result, Hf and Zr oxyfluorides may be useful protective coatings in both oxygen and fluorine-based plasma environments.

Many techniques have been examined to deposit metal oxyfluorides, such as solgel,[18] sputtering,[19–22] spray coating,[23] and metalorganic chemical vapor deposition.[24] However, the major bottleneck of these techniques is nonuniform deposition, especially on three-dimensional and high aspect ratio structures. A promising alternate technique that can deposit highly conformal and pinhole-free thin films is atomic layer deposition (ALD).[25–27] ALD is closely related to chemical vapor deposition and is defined by two sequential, self-limiting surface chemical reactions.[27]

Many investigations have reported that ALD can deposit corrosion protection coatings. Previous studies include TiO_2, Al_2O_3, and other metal oxide ALDs for copper,[28,29] Al_2O_3 ALD for aluminum,[30,31] Al_2O_3 and TiO_2 ALD for steel,[31–34] and Al_2O_3 and TiO_2 ALD for polymers.[35,36] ALD has been extensively developed for various binary compounds.[37] ALD can also be extended to a variety of ternary and quaternary materials.[37] To date, aluminum oxyfluoride (AlO_xF_y) is the only metal oxyfluoride that has been developed using ALD techniques.[13]

Hafnium oxide (HfO_2) ALD and hafnium fluoride (HfF_4) ALD were used for hafnium oxyfluoride ALD. HfO_2 ALD has been developed with various hafnium precursors.[38–43] In this paper, HfO_2 ALD was performed at 150 °C with a growth rate of 1.1 Å/cycle using alternating exposures of tetrakis(dimethylamido) hafnium (TDMAH) and H_2O as the metal and oxygen sources, respectively.[42,43] Similarly, HfF_4 ALD was performed using alternating exposures of TDMAH and HF.[44] The deposition temperature for HfF_4 ALD was 150 °C with a growth rate of 1.2 Å/cycle.

Zirconium oxyfluoride ALD was also demonstrated using zirconium oxide (ZrO_2) ALD and zirconium fluoride (ZrF_4) ALD. ZrO_2 ALD has been accomplished using water (H_2O) as the oxygen source and a variety of zirconium precursors.[38,45–47] In this paper, ZrO_2 ALD was performed using alternating exposures of tetrakis(ethylmethylamido)zirconium (TEMAZ) and H_2O.[38,45] The growth rate using TEMAZ and H_2O at 150 °C was 0.9 Å/cycle. Similarly, ZrF_4 was performed using TEMAZ and HF as the reactants.[44] The growth rate was 1.1 Å/cycle at 150 °C.

In this work, two pathways were used to deposit HfO_xF_y and ZrO_xF_y films with tunable stoichiometry: the nanolaminate method and the HF exchange method.[13] The nanolaminate method is defined by the sequential deposition of MO_x ALD and MF_y ALD layers. The HF exchange method is based on the thermodynamically favorable fluorination of MO_x by HF. *In situ* quartz crystal microbalance (QCM) studies were utilized to understand the growth mechanism during both deposition methods. Compositional tunability was verified using *ex situ* Rutherford backscattering spectroscopy (RBS) measurements. The physical sputtering rates of MO_xF_y thin films were determined during x-ray photoelectron spectroscopy (XPS) depth profiling.

II. EXPERIMENT

A. ALD reactor with *in situ* QCM

The ALD of HfO_xF_y and ZrO_xF_y thin films was investigated in a custom-built, hot wall, laminar flow reactor at 150 °C.[13,48] TDMAH (Strem Chemicals), water (HPLC grade H_2O, Sigma Aldrich), and HF-pyridine (70% wt. HF, Sigma Aldrich) were used as the hafnium, oxygen, and fluorine sources for HfO_xF_y deposition, respectively. Similarly, TEMAZ (Strem Chemicals) was used as the zirconium source, while water and HF-pyridine were used

as the oxygen and the fluorine sources for ZrO_xF_y deposition, respectively. All the precursors were used as received without any further processing. TDMAH and TEMAZ were transferred using a dry N_2-filled glove bag and kept in a stainless steel container. HF-pyridine was also transferred using a dry N_2-filled glove bag and kept in a gold-coated stainless steel container.

TDMAH and TEMAZ were heated to ~68 and ~110 °C, respectively, to generate sufficient vapor pressure throughout the deposition process. H_2O and HF were maintained at room temperature at all times. The deposition chamber was held at 150 °C using ceramic heaters controlled by a proportional-integral-derivative (PID) temperature controller (2604, Eurotherm). This controller maintained the set point temperature to within ±0.04 °C. All the precursors entered the deposition chamber through precursor lines that were progressively heated from the precursor source to the reactor.

A mechanical rotary vane pump (Pascal 2010SD, Pfeiffer Vacuum) was used to control the base pressure of the reactor. The base pressure was maintained at ~1 Torr using a 200 SCCM flow of high purity argon gas (Ar, Airgas, prepurified) provided by mass flow controllers (Type 1179A, MKS). Pressure transients were measured using a bakeable capacitance manometer (Baratron 121A, MKS). An activated alumina trap (Visi-trap, LACO technologies) was connected at the inlet of the vacuum pump to trap the unreacted precursors. Additionally, the exhaust of the vacuum pump was passed through a calcium oxide solution to remove any unreacted precursors such as HF.

The growth mechanism during metal oxyfluoride ALD was investigated using an *in situ* QCM at 150 °C in the reactor.[13,48] A gold-coated, polished AT cut quartz crystal with an ~6 MHz resonance frequency (Colorado Crystal Corp.) was used as the QCM sensor. The quartz crystal was sealed using high temperature epoxy (Epo-Tek H21D, Epoxy Technology) in a commercially available, bakeable crystal drawer and retainer assembly (BSH-150, Inficon). Further precaution was taken to avoid any deposition on the back of the quartz crystal by maintaining an additional Ar flow through the QCM assembly.[48] This additional Ar flow increased the reactor pressure by 0.1 Torr above base pressure.

Frequency fluctuations during the deposition were recorded using a QCM monitor (Maxtek TM-400, Inficon). These frequency changes were converted to mass changes using the Sauerbrey equation. The bare QCM crystal was first coated with 200 cycles of Al_2O_3 ALD at 150 °C before starting any experiment. Trimethyl aluminum (97%, Sigma Aldrich) and water (HPLC grade H_2O, Sigma Aldrich) were used as the aluminum and oxygen sources, respectively, for Al_2O_3 ALD.

B. MO_xF_y growth methods

MO_xF_y ALD was performed with two different methods. Figures 2(a) and 2(b) illustrate the nanolaminate method and the HF exchange method, respectively. During the nanolaminate method shown in Fig. 2(a), the MO_xF_y ALD films were grown using sequential deposition of "n" cycles of MO_x ALD and "m" cycles of MF_y ALD where "M" signifies Hf and Zr. The relative concentrations of oxygen and fluorine in the MO_xF_y thin films were controlled by varying the "n:m" ratio. One supercycle during the nanolaminate method is defined as a combination of "n" cycles of MO_x and "m" cycles of MF_y.

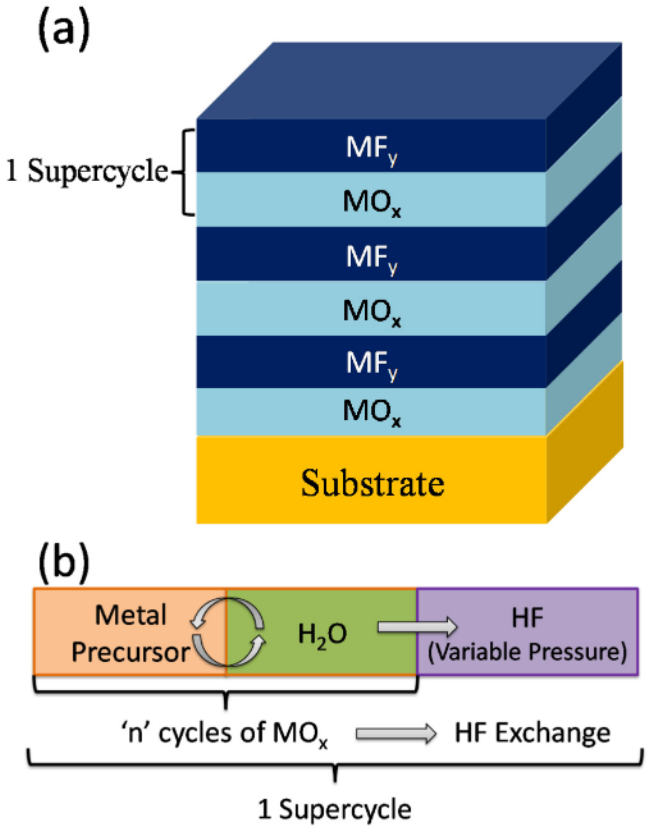

FIG. 2. Schematic of MO_xF_y ALD using (a) the nanolaminate method and (b) the HF exchange method.

The typical dosing sequence during nanolaminate growth of HfO_xF_y is designated as $(2\text{-}45\text{-}0.3\text{-}45)_n\text{-}(2\text{-}45\text{-}0.5\text{-}45)_m$ representing $(TDMAH\text{-}Ar\text{-}H_2O\text{-}Ar)_n\text{-}(TDMAH\text{-}Ar\text{-}HF\text{-}Ar)_m$. The times are in seconds during this "n:m" sequential HfO_2 ALD and HfF_4 ALD dosing sequence. The partial pressures of TDMAH, H_2O, and HF were 20, 50, and 20–25 mTorr, respectively, unless stated otherwise. The dosing sequence during nanolaminate growth of ZrO_xF_y is designated as $(0.3\text{-}45\text{-}0.3\text{-}45)_n\text{-}(0.3\text{-}45\text{-}0.5\text{-}45)_m$ representing $(TEMAZ\text{-}Ar\text{-}H_2O\text{-}Ar)_n\text{-}(TEMAZ\text{-}Ar\text{-}HF\text{-}Ar)_m$. The partial pressures were 5–10, 50, and 20–25 mTorr for TEMAZ, H_2O, and HF, respectively, unless stated otherwise. The precursor dose times were sufficient for the reactions to be in the saturation limit based on mass change versus dose time.

MO_xF_y deposition was also performed using the HF exchange method, as illustrated in Fig. 2(b). This deposition mechanism is based on the deposition of "n" cycles of MO_x ALD followed by fluorination using HF as the fluorinating agent. The combination of "n" cycles of MO_x ALD and fluorination defines one supercycle. The supercycle is denoted as "n:m" where "n" is the number of MO_x ALD cycles and "m" is the number of HF doses. The dosing

sequence during HF exchange growth of HfO_xF_y is designated as $(2\text{-}45\text{-}0.3\text{-}45)_n\text{-}(0.3\text{-}45)_m$ where the precursor sequence is $(TDMAH\text{-}Ar\text{-}H_2O\text{-}Ar)_n\text{-}(HF\text{-}Ar)_m$. Similarly, $(0.3\text{-}45\text{-}0.3\text{-}45)_n\text{-}(0.5\text{–}45)_m$ is the dosing sequence during HF exchange growth of ZrO_xF_y with the precursor sequence of $(TEMAZ\text{-}Ar\text{-}H_2O\text{-}Ar)_n\text{-}(HF\text{-}Ar)_m$.

The fluorination reactions of HfO_2 and ZrO_2 by HF are given by

$$HfO_2 + 4\ HF(g) \rightarrow HfF_4 + 2\ H_2O(g), \quad (1)$$

$$ZrO_2 + 4\ HF(g) \rightarrow ZrF_4 + 2\ H_2O(g). \quad (2)$$

These fluorination reactions are thermodynamically spontaneous with a standard Gibb's free energy change of $\Delta G° = -23$ and -21.5 kcal/mol for HfO_2 and ZrO_2, respectively, at 150 °C.[49] Similar fluorination of HfO_2 and ZrO_2 is possible using F_2 as the fluorine reactant.[50]

C. Compositional and structural analyses using XPS, RBS, and GIXRD

Compositional analysis was performed using MO_xF_y films with a thickness of ~30 nm that were deposited on Si (111) substrates at 150 °C. The Si (111) substrates had dimensions of 1×1 in.^{2}. Depth-profile XPS analysis revealed the elemental distribution in the various MO_xF_y thin films. The depth profiling of the films was also employed to calculate the physical sputtering rate using Ar^+ ions at 3 keV. The XPS data were collected with a commercial XPS instrument (PHI 5600, RBD Instruments) using the AugerScan software package (AugerScan, RBD Instruments). The XPS analysis was performed using the CASAXPS software package (Casa Software).

The MO_xF_y thin films were also investigated using RBS measurements to evaluate the precise compositions under various deposition conditions. All RBS spectra measurements and analysis were performed at the Rutgers University Laboratory for Surface Modification. This RBS analysis employed a 2 MeV He^{++} beam positioned normal to the substrate surface. The detector was located at a scattering angle of 163°. The RBS spectral resolution was 20 keV. Fitting the RBS spectra was performed using SIMNRA software.

The film structure was evaluated using grazing incidence x-ray diffraction (GIXRD). These GIXRD measurements were performed using a high resolution x-ray diffractometer (Bede D1, Jordan Valley Semiconductors) having Cu Kα (λ = 1.540 Å) radiation. The x-ray tube filament voltage and current were 40 kV and 35 mA, respectively. The HfO_2, ZrO_2, HfF_4, and ZrF_4 ALD films and the HfO_xF_y and ZrO_xF_y oxyfluoride ALD films grown at 150 °C were all amorphous.

III. RESULTS AND DISCUSSION

A. MO_xF_y films using the nanolaminate method

Figure 3 shows the mass changes recorded by the *in situ* QCM during ten consecutive supercycles of nanolaminate growth for 5:1 HfO_2:HfF_4 at 150 °C. Nanolaminate deposition consisted of five cycles of HfO_2 ALD followed by one cycle of HfF_4 ALD during each supercycle. One 5:1 HfO_2:HfF_4 supercycle was defined by a pulsing sequence designated as $(2\text{-}45\text{-}0.3\text{-}45)_5\text{-}(2\text{-}45\text{-}0.5\text{-}45)_1$. Long purge times of 45 s were used between each precursor exposure to ensure complete removal of excess precursor and reaction products. Figure 3 reveals linear mass gain versus time throughout the ten supercycles of 5:1 nanolaminate growth. The mass gain per supercycle during 5:1 HfO_2:HfF_4 ALD was $\Delta m = 380\text{–}385$ ng/(cm^2 supercycle).

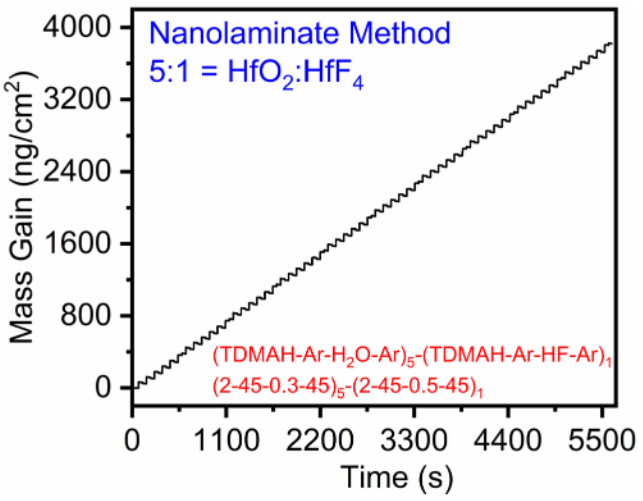

FIG. 3. Mass gain vs time recorded by QCM during 10 supercycles of 5:1 HfO_xF_y ALD using the nanolaminate method at 150 °C with a dosing sequence of $(2\text{-}45\text{-}0.3\text{-}45)_5\text{-}(2\text{-}45\text{-}0.5\text{-}45)_1$.

Figure 4 expands two consecutive supercycles from the linear growth regime of Fig. 3. In the first set of five cycles of HfO_2 ALD, the mass gain is highly digital and increases during TDMAH exposures and decreases during H_2O exposures. The total mass gain was $\Delta m_{HfO2} = 282\text{–}285$ ng/cm^2 after five cycles of HfO_2 ALD. Similarly, there were two distinct mass gains from the TDMAH exposure and the HF exposure during the HfF_4 ALD cycle. The total mass gain after one cycle of HfF_4 ALD was $\Delta m_{HfF4} = 95\text{–}98$ ng/cm^2. As a result, the mass gain per supercycle was 380–385 ng/(cm^2 supercycle).

ZrO_xF_y nanolaminate growth using 5:1 ZrO_2:ZrF_4 ALD at 150 °C was also studied using *in situ* QCM measurements, as shown in Fig. 5. The mass gain versus time throughout the ten supercycles of 5:1 nanolaminate growth is linear. Figure 6 expands two consecutive supercycles from Fig. 5. The total mass gain after five cycles of ZrO_2 ALD was $\Delta m_{ZrO2} = 141\text{–}144$ ng/cm^2. The mass gain after the ZrF_4 ALD cycle was $\Delta m_{ZrF4} = 67\text{–}69$ ng/cm^2. The overall mass gain during the 5:1 ZrO_2:ZrF_4 supercycle was $\Delta m = \Delta m_{ZrO2} + \Delta m_{ZrF4} = 208\text{–}210$ ng/(cm^2 supercycle).

The growth of MO_xF_y using the nanolaminate method is dependent on the nucleation of HfF_4 ALD on HfO_2 and HfO_2 ALD on HfF_4. Figure 7 displays the nucleation of HfF_4 ALD on HfO_2 and HfO_2 ALD on HfF_4. Figure 7(a) shows the mass gain versus time during the first six cycles of HfF_4 ALD on the Hf-OH*

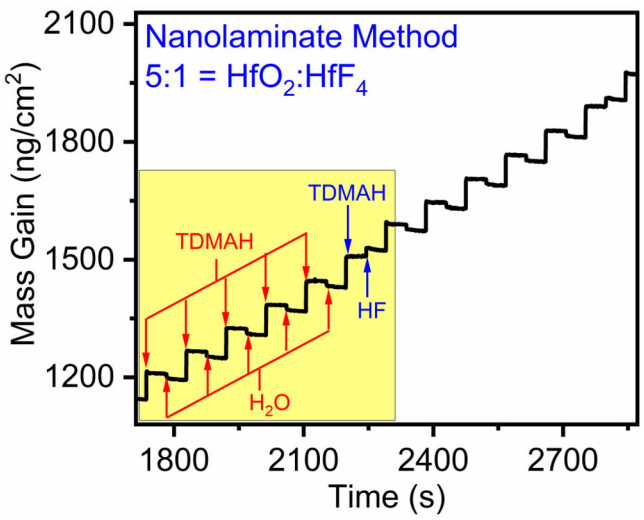

FIG. 4. Mass gain vs time recorded during two supercycles from a linear growth regime in Fig. 3.

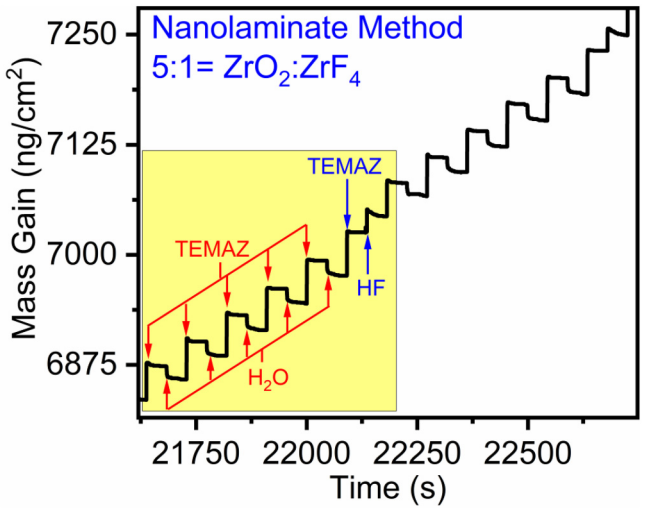

FIG. 6. Mass gain vs time recorded during two supercycles from a linear growth regime in Fig. 5.

terminated HfO_2 surface. The asterisk indicates the active surface species. The first cycle of HfF_4 ALD shows substantially higher mass gains during both the TDMAH and HF exposures than the mass gains observed during HfF_4 ALD in the steady state.

During the first HfF_4 ALD cycle on the Hf-OH* terminated HfO_2 surface, mass gains of 115 and 32 ng/cm^2 were recorded during TDMAH and HF exposures, respectively. The mass gain during the first TDMAH exposure results from TDMAH reaction with the Hf-OH* surface. The high mass gain during the first HF exposure is a combination of the HF reaction with Hf-NMe_2* species and the exchange reaction of F with O in the underlying HfO_2 film. The mass changes during subsequent TDMAH and HF exposures during HfF_4 ALD display substantially lower mass gains. From the second HfF_4 ALD cycle onward, the HfF_4 ALD displays steady-state HfF_4 ALD growth characteristics that have been observed earlier.[44] ZrF_4 ALD nucleation on the ZrO_2 surface is similar to HfF_4 ALD nucleation on the HfO_2 surface. The *in situ* mass changes during first six cycles of ZrF_4 ALD on the Zr-OH* terminated ZrO_2 surface are shown in Fig. 8(a).

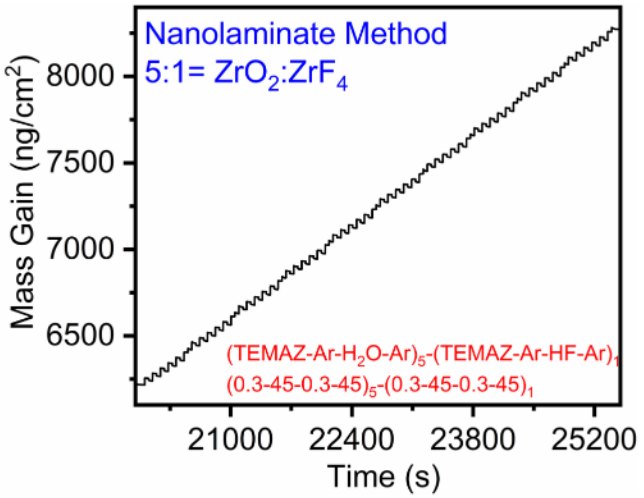

FIG. 5. Mass gain vs time recorded by QCM during ten supercycles of 5:1 ZrO_xF_y ALD using the nanolaminate method at 150 °C with a dosing sequence of $(0.3\text{-}45\text{-}0.3\text{-}45)_5\text{-}(0.3\text{-}45\text{-}0.5\text{-}45)_1$.

Figure 7(b) shows the mass gains versus time during the first six cycles of HfO_2 ALD on the Hf-F* terminated HfF_4 surface. The very first cycle of HfO_2 ALD shows lower mass gains than the mass gains observed during HfO_2 ALD in the steady state. During the first HfO_2 ALD cycle, mass gains of 61.8 and −14.5 ng/cm^2 occurred during the TDMAH and H_2O exposures, respectively. The mass gain during the first TDMAH exposure results from the TDMAH reaction with HF on the HfF_4 surface after the HF exposure. The mass loss during the first H_2O exposure can be identified as a combination of H_2O reaction with Hf-NMe_2* surface species and O exchange with F in Hf-F* surface species and in the underlying HfF_4 layer. As shown in Fig. 8(b), mass loss during the first H_2O exposure during ZrO_2 ALD nucleation on the Zr-F* terminated ZrF_4 surface can also be identified as a combination of H_2O reaction with the Zr-NEtMe* surface species and O exchange with F in Zr-F* surface species and in the underlying ZrF_4 layer.

The O exchange reaction with F can be described by

$$HfF_4 + 2\,H_2O(g) \rightarrow HfO_2 + 4\,HF(g). \quad (3)$$

The O to F conversion reaction is not predicted to be thermodynamically favorable at standard state with a Gibb's free energy of

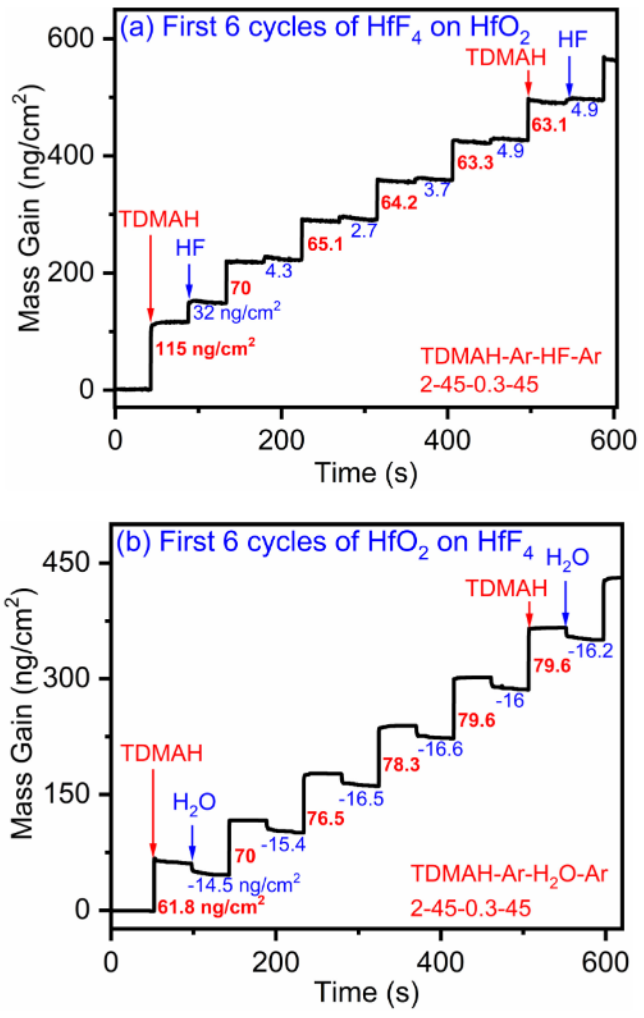

FIG. 7. Mass gain vs time recorded during the first six ALD cycles of (a) HfF_4 on Hf-OH* terminated HfO_2 surface and (b) HfO_2 on Hf-F* terminated HfF_4 surface at 150 °C.

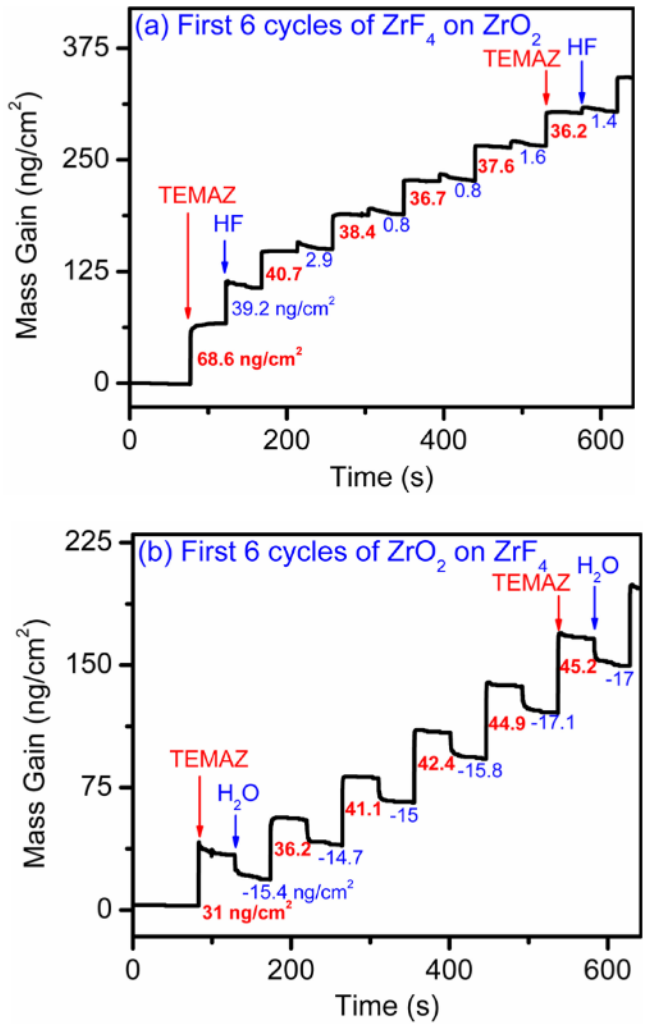

FIG. 8. Mass gain vs time recorded during the first six ALD cycles of (a) ZrF_4 on Zr-OH* terminated ZrO_2 surface and (b) ZrO_2 on Zr-F* terminated ZrF_4 surface at 150 °C.

$\Delta G° = +22.66$ kcal at 150 °C.[49] However, the experimental conditions are far from the assumption of standard state. The mass characteristics during the subsequent TDMAH and H_2O exposures from the second HfO_2 ALD cycle onward display steady-state HfO_2 ALD growth characteristics that have been observed earlier.[44]

Compositional analysis of the MO_xF_y thin films was studied with depth-profile XPS and RBS analyses. Depth-profile XPS was used only to validate the uniform distribution of all elements throughout the film. Because of preferential sputtering of fluorine and oxygen as compared to the metal cations (Hf and Zr) during XPS depth profiling, RBS analysis was used to determine the composition of the MO_xF_y thin films. Figure 9 displays the RBS profile for HfO_xF_y and ZrO_xF_y films with a thickness of ~30 nm grown using the 5:1 nanolaminate method on Si (111) at 150 °C.

Figure 9(a) shows the RBS profile of the HfO_xF_y thin film in the energy range of 200–1500 keV. This RBS profile reveals three distinct peaks at energies of 1275, 725, and 850 keV corresponding to Hf, O, and F, respectively. The elemental composition from the RBS analysis for the 5:1 nanolaminate growth is consistent with $HfO_{1.27}F_{1.46}$. Figure 9(b) shows the RBS profile of the ZrO_xF_y thin film in the energy range of 200–1300 keV. This RBS profile shows three peaks at energies 1200, 725, and 850 keV consistent with Zr, O, and F peaks, respectively. The elemental composition analysis for the 5:1 nanolaminate growth was $ZrO_{1.27}F_{1.46}$. Carbon and nitrogen are below the detection limit of the RBS spectrum.

The compositional tunability of the HfO_xF_y and ZrO_xF_y thin films was determined by RBS analysis with respect to various deposition conditions using the nanolaminate method, as shown in Fig. 10.

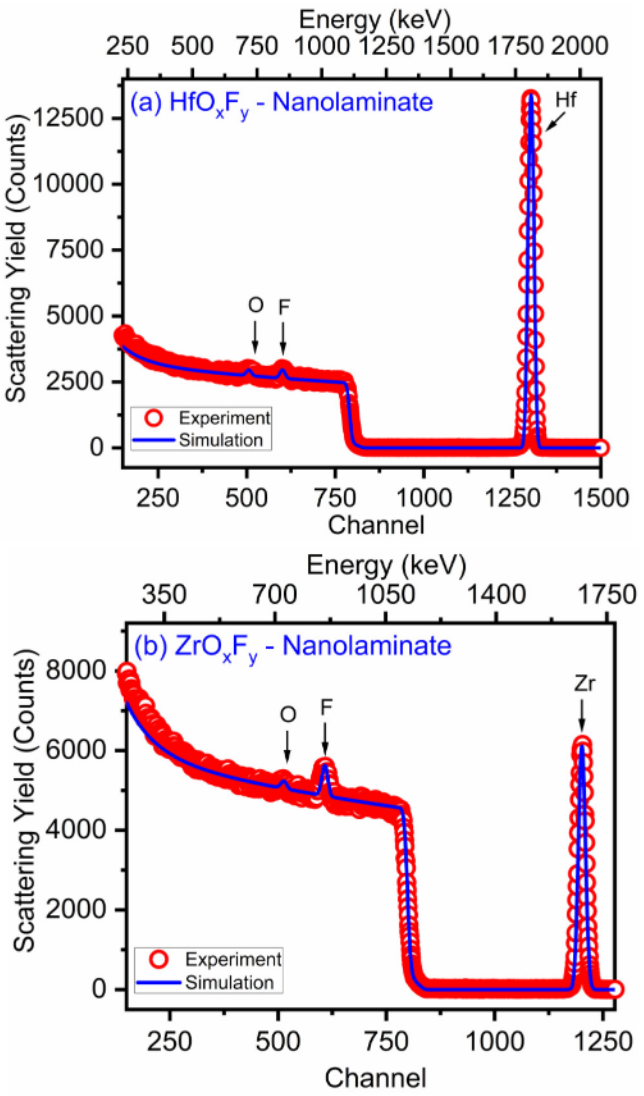

FIG. 9. RBS spectrum from ~30 nm films of (a) HfO_xF_y and (b) ZrO_xF_y grown by the 5:1 nanolaminate method on an Si(111) substrate at 150 °C.

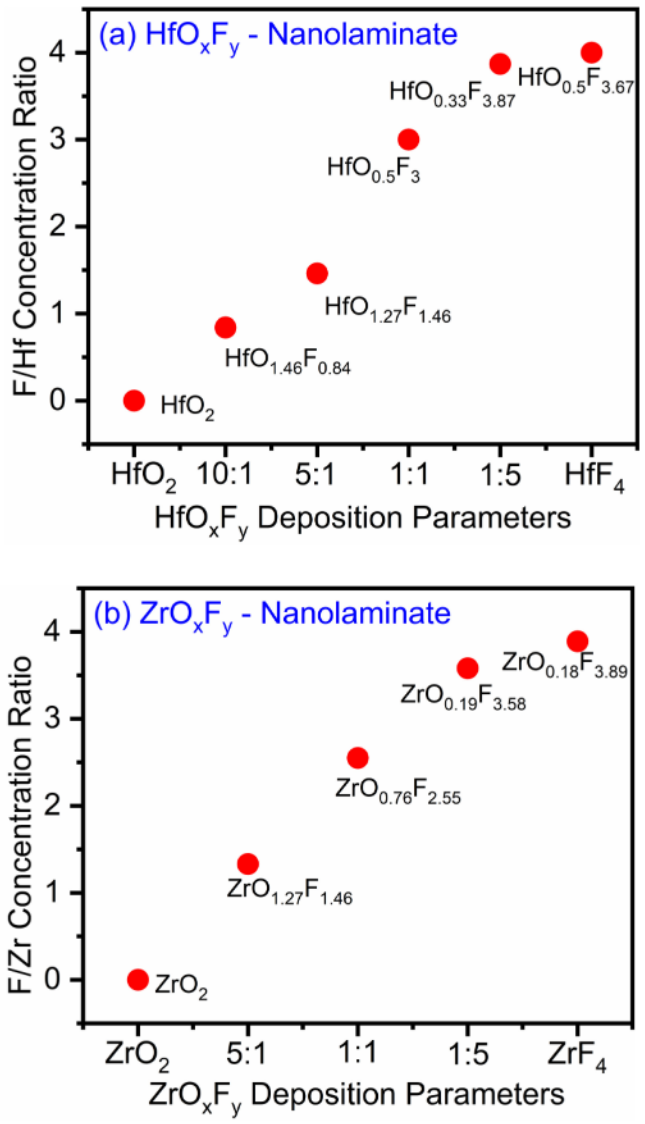

FIG. 10. Compositional tunability measured by RBS analysis for (a) HfO_xF_y and (b) ZrO_xF_y films deposited using the nanolaminate method at 150 °C.

The F/Hf concentration ratios of 0 and 3.87 are observed for HfO_2 and HfF_4, respectively. Intermediate F/Hf concentration ratios are observed for HfO_2:HfF_4 ALD cycle ratios of 10:1, 5:1, 1:1, and 1:5, as shown in Fig. 10(a). Similarly, F/Zr concentration ratios of 0 and 3.89 are observed for ZrO_2 and ZrF_4, respectively. Intermediate F/Zr concentration ratios are observed for 5:1, 1:1, and 1:5 ZrO_xF_y thin films, as shown in Fig. 10(b). Figure 10 confirms that a wide range of oxygen-to-fluorine concentrations can be achieved based on various deposition parameters using the nanolaminate method.

Table I summarizes the compositions of the various HfO_xF_y and ZrO_xF_y thin films grown by the nanolaminate method at 150 °C. The compositions are given from both XPS and RBS analyses. The compositions from XPS analysis are not accurate because of preferential sputtering during depth profiling. The compositions from RBS are consistent with an Hf oxidation state of 4+. The 5:1 and 1:1 HfO_2:HfF_4 nanolaminates yield an oxidation state of 4+. The 10:1 and 1:5 HfO_2:HfF_4 nanolaminates show slightly lower and slightly higher oxidation states of Hf than 4+. Deviations from an Hf oxidation state of 4+ may result from nonstoichiometric compositions in the HfO_xF_y thin films at the interfaces between the HfO_2 and the HfF_4 layers. The ZrO_xF_y thin films are consistent with an Zr oxidation state of 4+ for all the ZrO_xF_y films grown by the nanolaminate method.

TABLE I. Compositional analyses by XPS and RBS together with the respective sputtering rates for HfO_xF_y and ZrO_xF_y samples grown by the nanolaminate method at 150 °C.

Deposition condition	Composition		Rate of sputtering (Å/s)
	XPS	RBS	
HfO_2	HfO_1	$HfO_{2.00}$	0.07
HfF_4	$HfO_{0.07}F_{2.00}$	$HfO_{0.5}F_{3.67}$	0.25
ZrO_2	$ZrO_{1.13}$	ZrO_2	0.05
ZrF_4	$ZrO_{0.15}F_{1.8}$	$ZrO_{0.18}F_{3.89}$	0.23
HfO_xF_y by the nanolaminate method			
10:1	$HfO_{0.89}F_{0.3}$	$HfO_{1.46}F_{0.84}$	0.1
5:1	$HfO_{0.8}F_{0.55}$	$HfO_{1.27}F_{1.46}$	0.13
1:1	$HfO_{0.45}F_{1.2}$	$HfO_{0.5}F_{3.00}$	0.14
1:5	$HfO_{0.3}F_{1.5}$	$HfO_{0.33}F_{3.87}$	0.16
ZrO_xF_y by the nanolaminate method			
5:1	$ZrO_1F_{0.5}$	$ZrO_{1.27}F_{1.46}$	0.09
1:1	$ZrO_{0.6}F_{0.9}$	$ZrO_{0.76}F_{2.55}$	0.1
1:5	$ZrO_{0.26}F_{1.4}$	$ZrO_{0.19}F_{3.58}$	0.21

B. MO_xF_y films using the HF exchange method

MO_xF_y thin films were also deposited using the HF exchange method, as depicted in Fig. 2(b). Figure 11 shows the mass changes recorded by *in situ* QCM measurements during 25 consecutive supercycles of 1:1 HfO_xF_y ALD using the HF exchange method at 150 °C. The reaction sequence during this 1:1 HF exchange supercycle consisted of one cycle of HfO_2 ALD followed by a single HF exposure. This pulsing sequence during the 1:1 HfO_xF_y supercycle is designated as $(2\text{-}45\text{-}0.3\text{-}45)_1\text{-}(0.5\text{-}45)_1$. Figure 11 displays a linear mass gain versus time during 25 consecutive HfO_xF_y ALD cycles.

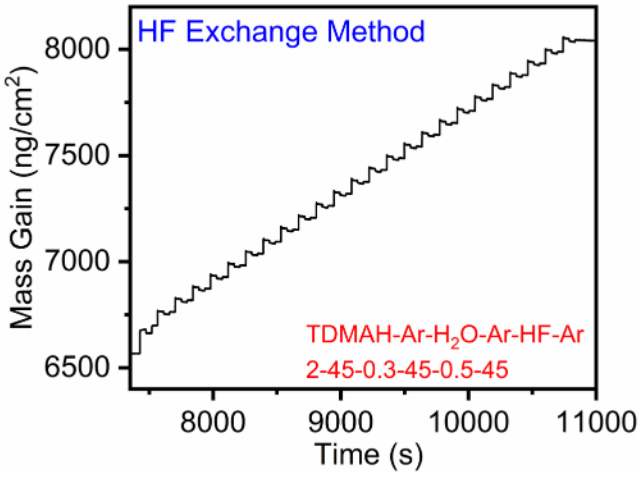

FIG. 11. Mass gain vs time recorded during 25 HfO_xF_y supercycles grown by the HF exchange method at 150 °C using a dosing sequence of (2-45-0.3-45-0.5-45).

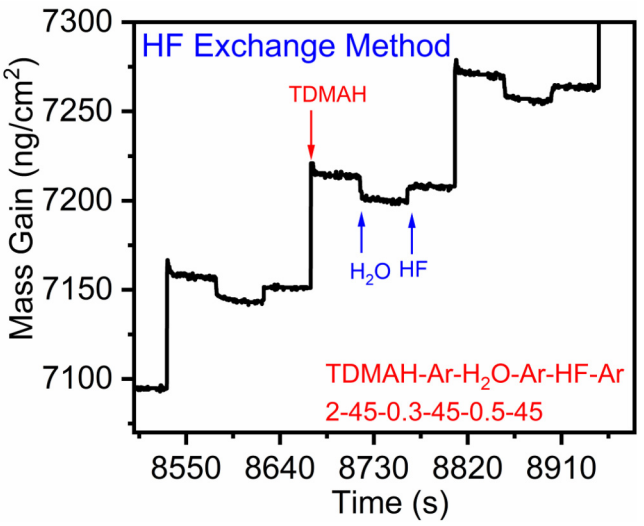

FIG. 12. Mass gain vs time recorded during three supercycles from a linear growth regime in Fig. 11.

The overall mass gain per supercycle during 1:1 HfO_xF_y ALD was $\Delta m = 55\text{–}56$ ng/(cm^{2}supercycle).

Figure 12 shows three consecutive supercycles from the linear growth regime of Fig. 11. A mass gain after TDMAH exposure of $\Delta m_{TDMAH} = 62\text{–}63$ ng/cm^2 and mass loss after H_2O exposure of $\Delta m_{H2O} = -13$ to 14 ng/cm^2 were observed during the HfO_2 ALD cycle. When HF was introduced after the HfO_2 ALD cycle at a pressure of 20 mTorr, a mass gain of $\Delta m_{HF} = 7\text{–}8$ ng/cm^2 was observed during the fluorination reaction. The overall mass gain per supercycle during the 1:1 HfO_xF_y supercycle was $\Delta m = \Delta m_{HfO2} + \Delta m_{HF} = 55\text{–}56$ ng/(cm^{2}supercycle).

For comparison, 25 consecutive supercycles of 1:1 ZrO_xF_y ALD by the HF exchange method at 150 °C are shown in Fig. 13. Figure 14 shows an expansion of three consecutive supercycles from the linear growth regime of Fig. 13. The mass changes are similar to 1:1 HfO_xF_y ALD by the HF exchange method. The overall mass gain during the 1:1 ZrO_xF_y supercycle was $\Delta m = 29\text{–}31$ ng/(cm^2 supercycle).

The composition of the MO_xF_y thin films was studied by RBS analysis. Figure 15 shows the RBS profile of the HfO_xF_y and ZrO_xF_y films with a thickness of ~ 30 nm grown the 1:1 HF exchange method on Si (111) at 150 °C. Figure 15(a) shows the RBS profile for the 1:1 HfO_xF_y film in the energy range of 200–1500 keV. This RBS profile displays peaks corresponding to Hf, O, and F at energies of 1275, 725, and 850 keV, respectively. Based on the RBS peak fitting, the composition of the 1:1 HfO_xF_y film was $HfO_{0.84}F_{2.45}$. The RBS profile of the 1:1 ZrO_xF_y film is displayed in Fig. 15(b). The three distinct peaks at energies of 1200, 725, and 850 keV correspond to Zr, O, and F, respectively. The composition of the 1:1 ZrO_xF_y thin film was $ZrO_{0.71}F_{2.24}$.

Compositional variations in the MO_xF_y thin films grown by the HF exchange method can be obtained by changing the HF

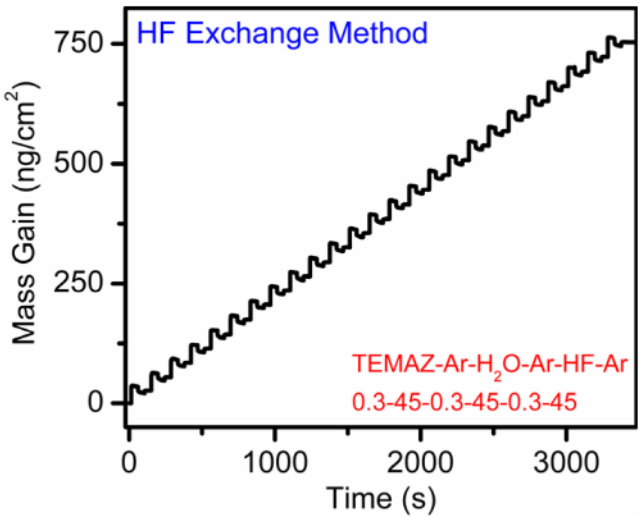

FIG. 13. Mass gain vs time recorded during 25 ZrO_xF_y supercycles grown by the HF exchange method at 150 °C using a dosing sequence of (0.3-45-0.3-45-0.5-45).

pressure during the fluorination reaction or by varying the number of MO_x ALD cycles prior to the HF fluorination reaction. To evaluate the effect of HF pressure, the HF pressure was varied in the range of 20–200 mTorr using HfO_2 or ZrO_2 ALD layers grown using five ALD cycles. The mass gains during the fluorination increased progressively with HF pressure similar to earlier results for the fluorination of Al_2O_3 by HF.[13]

Figure 16 shows the effect of the underlying MO_x ALD film thickness on the fluorination of both HfO_2 and ZrO_2. The MO_x

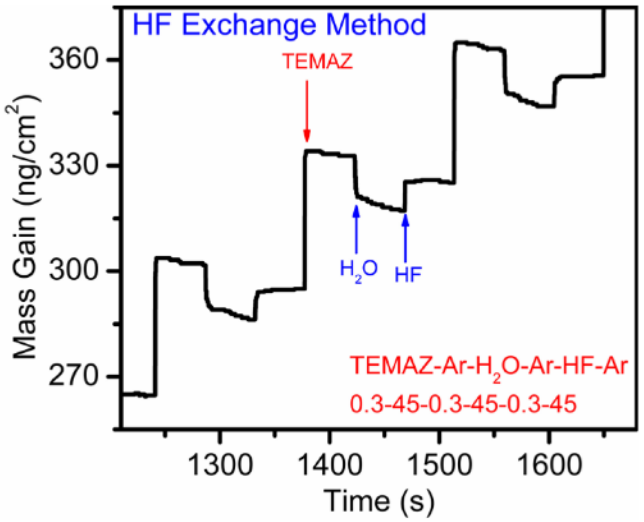

FIG. 14. Mass gain vs time recorded during three supercycles from a linear growth regime in Fig. 13.

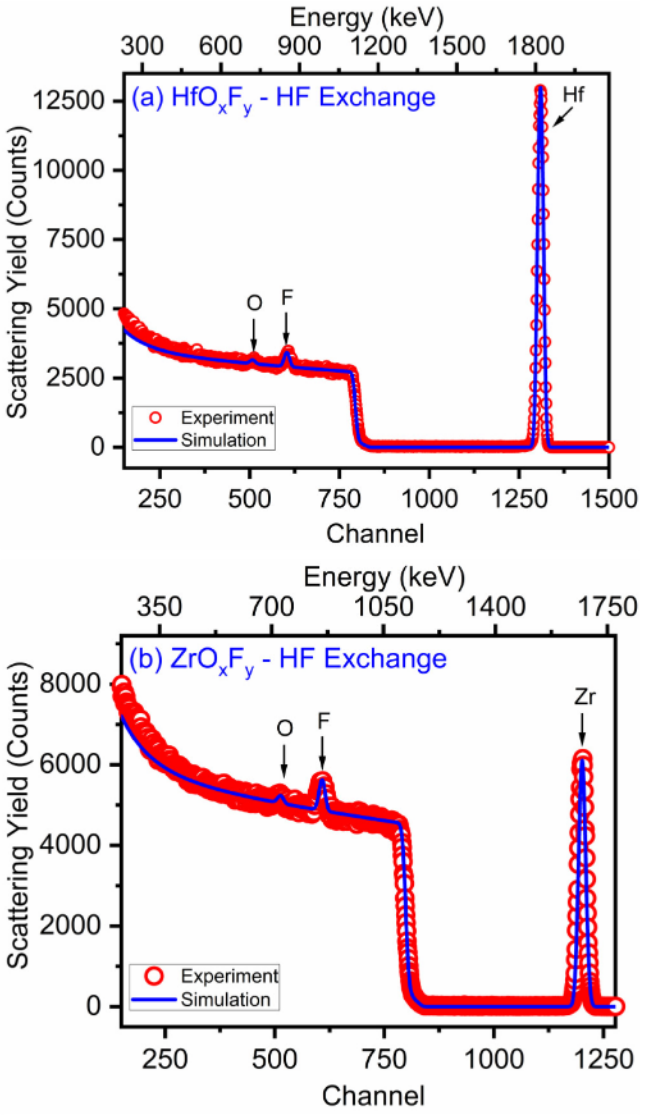

FIG. 15. RBS spectrum of ~30 nm films of (a) HfO_xF_y and (b) ZrO_xF_y grown by the 1:1 HF exchange method on an Si(111) substrate at 150 °C.

ALD film thickness was defined by 5, 50, and 200 MO_x ALD cycles. The HF pressure was kept constant at 20 mTorr. Figure 16(a) reveals that the mass gains during HF exposure were $\Delta m_{HF} = 25–28$ ng/cm^2 for five HfO_2 ALD cycles. Likewise, the mass gains increased to $\Delta m_{HF} = 42–45$ ng/cm^2 for 50 and 200 HfO_2 ALD cycles. For ZrO_2 ALD, Fig. 16(b) shows that mass gains of $\Delta m_{HF} = 25–28$ ng/cm^2 were observed during HF exposure for five ZrO_2 ALD cycles. Higher mass gains of $\Delta m_{HF} = 65–70$ ng/cm^2 were measured during HF exposure for 50 and 200 ZrO_2 ALD cycles. The higher Δm_{HF} values for the thicker ALD films indicate that the HF exchange reaction is not limited to the surface of the ALD films. HF is able to diffuse into

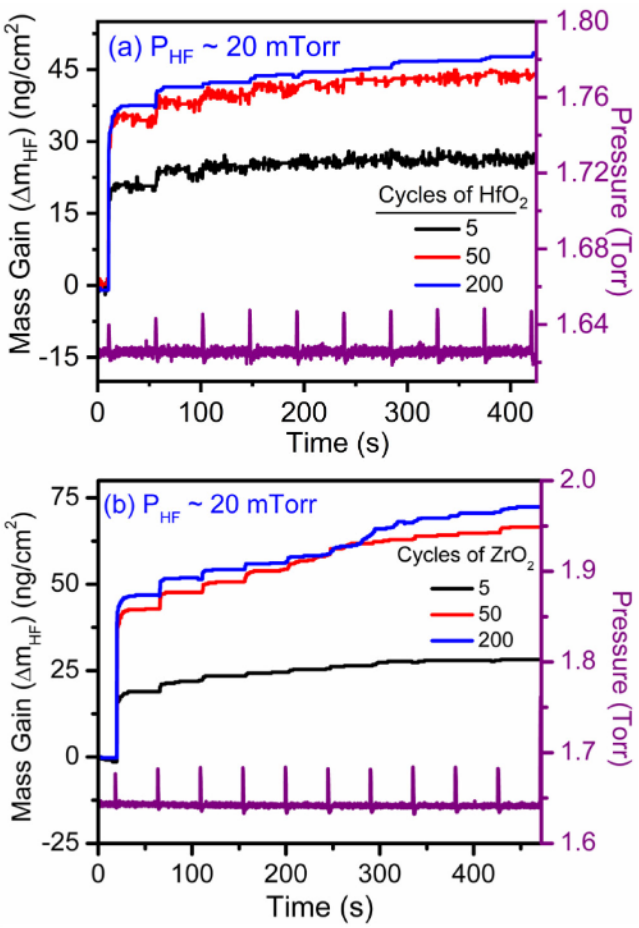

FIG. 16. Effect of the underlying MO_x thickness on a fluorination reaction measured by mass gain (Δm_{HF}) vs the number of HF doses during (a) HfO_xF_y and (b) ZrO_xF_y ALD by using the HF exchange method at 150 °C.

the HfO_2 and ZrO_2 ALD films. The fluorination depth in the ALD films is limited to a film thickness no larger than the thickness defined by 50 ALD cycles.

The mass changes during fluorination can be utilized to estimate the minimum fluorine penetration depth in the HfO_2 or ZrO_2 ALD films assuming complete conversion to HfF_4 or ZrF_4. Based on the reaction $HfO_2 + 4\ HF\ (g) \rightarrow HfF_4 + 2\ H_2O\ (g)$ given in Eq. (1), the mass gain $\Delta m_{HF} = 45\ ng/cm^2$ is consistent with the conversion of 1.02×10^{-9} mol/cm^2 of HfO_2 to HfF_4. The mass of this HfF_4 layer is 2.6×10^{-7} g/cm^2. This HfF_4 mass corresponds to an HfF_4 film thickness of 3.6 Å given an HfF_4 density of 7.1 g/cm^3. Similarly, the mass gain $\Delta m_{HF} = 65\ ng/cm^2$ is consistent with the conversion of 1.48×10^{-9} mol/cm^2 of ZrO_2 to ZrF_4. The mass of this ZrF_4 layer is 2.5×10^{-7} g/cm^2. This ZrF_4 mass corresponds with a ZrF_4 film thickness of 5.6 Å given a ZrF_4 density of 4.43 g/cm^3.

Fluorine diffusion into the ALD layers is another factor that may affect the amount of fluorination. If F can diffuse into the ALD layer, then more F may be able to be absorbed at the surface of the ALD layer. To test for F diffusion, HF was exposed to the ALD layer after different aging times at 150 °C. The aging times were 30 min, 1 h, 2 h, and 3.5 h. The increasing *in situ* QCM mass changes with aging times indicated that F diffusion occurs in the ALD layer at 150 °C. Similar results were observed earlier for F diffusion into Al_2O_3 ALD layers.[13]

The compositional tunability of the HfO_xF_y and ZrO_xF_y films determined by RBS analysis using the HF exchange method is shown in Fig. 17. Figure 17(a) displays the compositional tunability of the HfO_xF_y films with respect to various deposition conditions. Intermediate F/Hf concentration ratios of 0.24, 1.5, and 2.45 are observed for HfO_2 ALD cycle:HF exposure ratios of 50:10, 5:10, and 1:1, respectively. Figure 17(b) represents the F/Zr concentration ratios for various ZrO_xF_y films grown by the HF exchange method. Intermediate F/Zr concentration ratios of 0.36, 1.81, and 2.24 are observed for the 50:10, 5:10, and 1:1 ZrO_xF_y films, respectively. Table II tabulates the compositions of various HfO_xF_y and ZrO_xF_y films grown using the HF exchange method from both XPS and RBS analyses. Preferential sputtering accounts for the differences between the compositions from XPS and RBS analyses.

C. Sputtering rates of MO_xF_y films

The physical sputtering rates of the various MO_xF_y films were evaluated during XPS depth profiling. The physical sputtering rate was defined according to the total thickness of the MO_xF_y film and the sputtering time,

$$\text{Physical sputtering rate} = \text{Thickness of } MO_xF_y \text{film/sputtering time.} \quad (4)$$

The thicknesses of all MO_xF_y films were constant at ~30 nm. The sputtering time was the time required to reach the silicon substrate surface. This sputtering time was defined when the Si 2p intensity reached 50% of the total atomic concentration.[6,13,51] The physical sputtering rates of pure metal oxides and metal fluorides were determined to be 0.07, 0.05, 0.25, and 0.23 Å/s for HfO_2, ZrO_2, HfF_4, and ZrF_4, respectively. The physical sputtering rates of the metal fluorides are significantly higher than the physical sputtering rates of their metal oxide counterparts.

Figures 18 and 19 display the physical sputtering rates as a function of the F/Hf and F/Zr concentration ratio for the various HfO_xF_y and ZrO_xF_y films grown by the nanolaminate method and the HF exchange method, respectively. The F/Hf and F/Zr ratios were determined from RBS analysis. The physical sputtering rates progressively increase at higher fluorine concentrations. A similar correlation was observed earlier for aluminum and yttrium oxides and fluorides.[6] The physical sputtering rates of the AlO_xF_y ALD films also progressively increased with fluorine concentration.[13] The sputtering rates for all the samples are tabulated in Tables I and II. The sputtering rates alone do not argue that oxyfluoride films are more resistant to fluorine or oxygen plasmas.

Higher physical sputtering rates at higher fluorine concentrations are consistent with the correlation between the physical sputtering rate and various parameters such as the boiling point

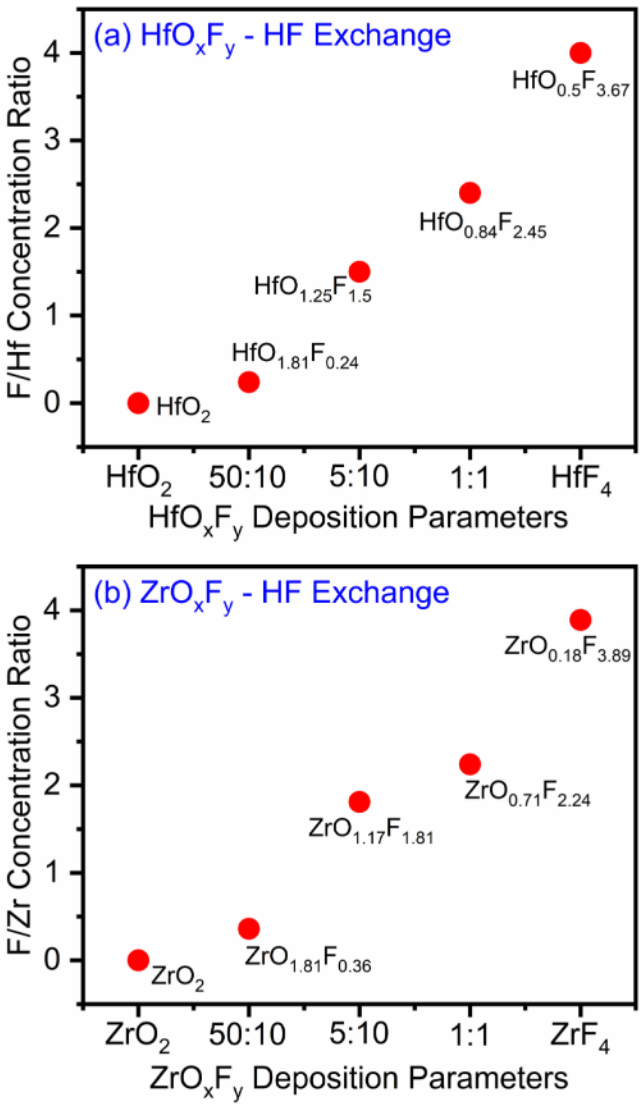

FIG. 17. Compositional tunability measured by RBS analysis for (a) HfO_xF_y and (b) ZrO_xF_y films deposited using the HF exchange method at 150 °C.

temperature and bond strengths.[6] The boiling temperatures of HfO_2 and ZrO_2 are 5400 and 4300 °C, respectively. In contrast, the boiling temperatures of HfF_4 and ZrF_4 are lower at 970 and 905 °C, respectively. The bond enthalpies of Hf–O and Zr–O bonds are ~802 and 776 kJ/mol, respectively. In contrast, the bond enthalpies of Hf–F and Zr–F bonds are lower at ~650 and 616 kJ/mol, respectively.

D. Oxyfluoride films as protective coatings

Fluorine-based plasma exposures to metal oxides, such as Y_2O_3, can fluorinate the oxide surface and produce particles.[8,10,11,16] Likewise, oxygen-containing plasma exposures to metal fluorides, such as YF_3, can oxidize and erode the fluorine surface.[7,8] Figure 1 shows the volume expansion and volume contraction as a result of the fluorination of metal oxides and the oxidation of metal fluorides, respectively. The effects of volume expansion and volume contraction also lead to compressive and tensile stress in the films, respectively. This film stress can cause particle generation, erosion, and film cracking.[7–10] Minimization of this stress in protective coatings is needed to enhance corrosion resistance in both oxygen and fluorine-containing plasma environments.

To assess various protective coating materials, the molar volume expansion ratio for the fluorination of the metal oxide to the metal fluoride can be used to compare the estimated strains induced in the metal oxide by fluorination. Table III presents the molar volumes of various metal oxides (MO_x) and metal fluorides (MF_y) along with the expansion ratio and estimated strain during fluorination of the metal oxide. The strain, ε, is defined as the change in length, Δl, divided by the initial length, l, or $\varepsilon = \Delta l/l$. The strain is determined from $\Delta l/l = (\text{molar volume expansion ratio})^{1/3} - 1$. The molecular weights and densities for the calculation of molar volumes are taken from the literature.[52]

Table III shows that the expansion ratio of Al_2O_3 to AlF_3 is the highest at a molar volume ratio of $2AlF_3/Al_2O_3 = 2.26$. This expansion ratio will produce a high strain value of $\varepsilon = \Delta l/l = 0.31$. In contrast, the expansion ratio of Y_2O_3 to $2YF_3$ is the one of the lowest in Table III at a molar volume ratio of $Y_2O_3/2YF_3 = 1.61$. This expansion ratio will produce a lower strain of $\varepsilon = \Delta l/l = 0.17$. Y_2O_3, YF_3, and YO_xF_y have frequently been studied as protective coatings.[7,14–16]

The expansion ratio of HfO_2 to HfF_4 and ZrO_2 to ZrF_4 have molar volume ratios of $HfO_2/HfF_4 = 1.66$ and $ZrO_2/ZrF_4 = 1.74$, respectively. These expansion ratios will generate strains of $\varepsilon = \Delta l/l = 0.18$ and 0.20 for the Hf and Zr systems, respectively. Based on these expansion ratios and strain values and their similarity to the values for Y_2O_3/YF_3, the HfO_xF_y and ZrO_xF_y oxyfluorides

TABLE II. Compositional analyses by XPS and RBS together with the respective sputtering rates for HfO_xF_y and ZrO_xF_y samples grown by the HF exchange method at 150 °C.

Deposition condition	Composition		Rate of sputtering (Å/s)
	XPS	RBS	
HfO_2	HfO_1	$HfO_{2.00}$	0.07
HfF_4	$HfO_{0.07}F_{2.00}$	$HfO_{0.5}F_{3.67}$	0.25
ZrO_2	$ZrO_{1.13}$	ZrO_2	0.05
ZrF_4	$ZrO_{0.15}F_{1.8}$	$ZrO_{0.18}F_{3.89}$	0.23
HfO_xF_y by the HF exchange method			
50:10	$HfO_{0.9}F_{0.08}$	$HfO_{1.81}F_{0.24}$	0.09
5:10	$HfO_{0.8}F_{0.5}$	$HfO_{1.25}F_{1.5}$	0.15
1:1	$HfO_{0.5}F_{1.1}$	$HfO_{0.84}F_{2.45}$	0.17
ZrO_xF_y by the HF exchange method			
50:10	$ZrO_{1.2}F_{0.12}$	$ZrO_{1.81}F_{0.36}$	0.09
5:10	$ZrO_{0.83}F_{0.64}$	$ZrO_{1.17}F_{1.81}$	0.11
1:1	$ZrO_{0.77}F_1$	$ZrO_{0.71}F_{2.24}$	0.16

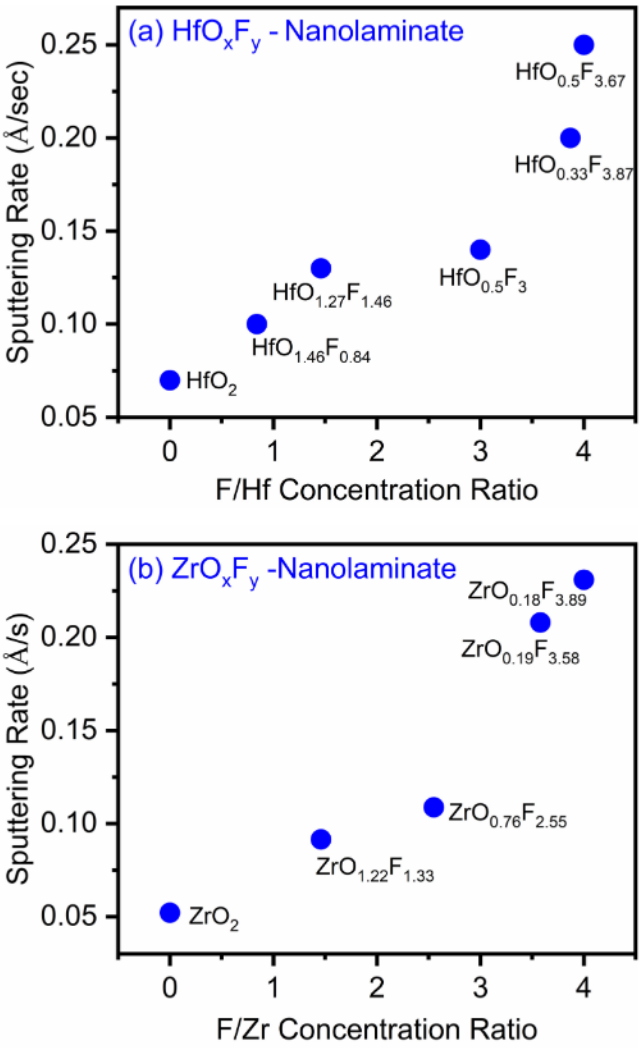

FIG. 18. Sputtering rate of (a) HfO_xF_y films with a variable F/Hf concentration ratio and that of (b) ZrO_xF_y films with a variable F/Zr concentration ratio grown by the nanolaminate method obtained from XPS depth profiling.

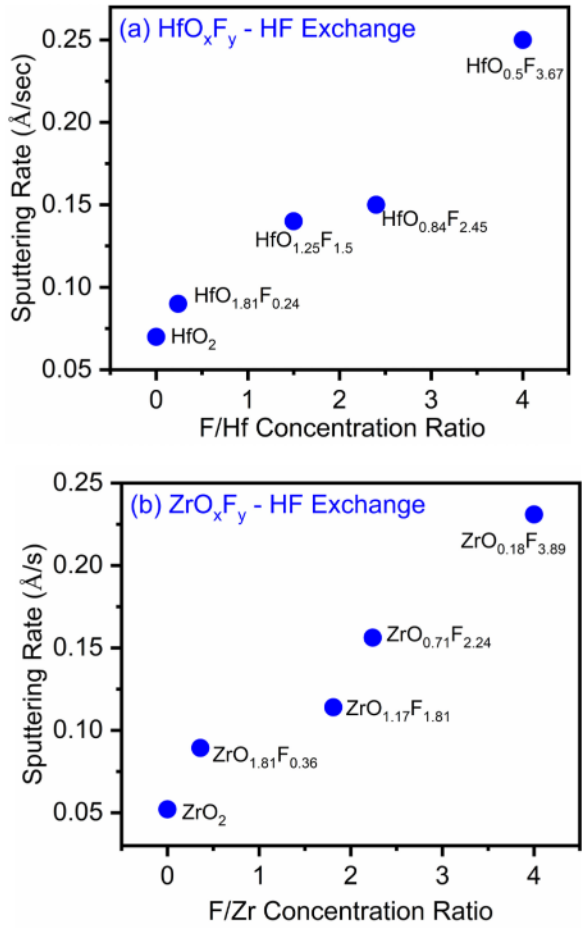

FIG. 19. Sputtering rate of (a) HfO_xF_y thin films with a variable F/Hf concentration ratio and that of (b) ZrO_xF_y films with a variable F/Zr concentration ratio grown by the HF exchange method as obtained from XPS depth profiling.

are potential materials for protective coatings in both fluorine and oxygen plasma environments. Other promising oxyfluorides with even lower strains include materials from the lanthanide series such as LaO_xF_y, ErO_xF_y, and GdO_xF_y.

The low expansion ratios for HfO_2 to HfF_4 and ZrO_2 to ZrF_4 lead to low compressive strains upon fluorination of the oxide. Similarly, low contraction ratios for HfF_4 to HfO_2 and ZrF_4 to ZrO_2 lead to low tensile strains upon oxidation of the fluoride. When considering hafnium and zirconium oxyfluoride films as protective coatings for exposure to both fluorine and oxygen-containing plasmas, the oxyfluorides with compositions in the middle of the range would serve as the best starting point. These oxyfluorides could then change composition to fluoride and oxide

TABLE III. Molar volume of various metal oxides and metal fluorides along with the metal oxide to metal fluoride expansion ratio and estimated strain.

Metal oxide (MO_x)	Molar volume (cm^3/mol)	Metal fluoride (MF_y)	Molar volume (cm^3/mol)	Expansion ratio (MF_y/MO_x)	Strain (ε)
Al_2O_3	25.81	AlF_3	29.16	2.26	0.31
Sc_2O_3	35.73	ScF_3	40.29	2.26	0.31
Nb_2O_3	57.78	NbF_5	57.11	1.98	0.26
ZrO_2	21.69	ZrF_4	37.74	1.74	0.2
HfO_2	21.74	HfF_4	36.05	1.66	0.18
Y_2O_3	45.07	YF_3	36.38	1.61	0.17
La_2O_3	50.05	LaF_3	33.2	1.33	0.099
Er_2O_3	44.28	ErF_3	28.68	1.29	0.089
Gd_2O_3	48.92	GdF_3	30.17	1.23	0.071

with minimum strain during exposure to fluorine or oxygen plasmas. Figure 10 for the nanolaminate method and Fig. 17 for the HF exchange method provide guidance for the compositional tuning of these oxyfluoride films.

IV. CONCLUSIONS

Hafnium and zirconium oxyfluoride thin films with tunable stoichiometry were grown with ALD techniques using TDMAH and TEMAZ as metal sources and H_2O and HF as the oxygen and fluorine precursors, respectively, at 150 °C. The nanolaminate method and the HF exchange method were employed to deposit the MO_xF_y (M = Hf, Zr) thin films. The nanolaminate method was defined by the sequential deposition of MO_x ALD and MF_y ALD layers. Compositional tunability was obtained by varying the ratio of the number of MO_x ALD cycles to the number of MF_y ALD cycles in the nanolaminate. In comparison, the HF exchange method was based on the thermodynamically favorable fluorination reaction of MO_x by HF. The composition could be tuned by varying the thickness of the initial MO_x ALD layer or the subsequent HF pressure.

The MO_xF_y growth mechanism was monitored using *in situ* QCM studies. Both the deposition methods demonstrated linear growth of MO_xF_y ALD at 150 °C. *Ex situ* RBS studies were utilized to study the composition of the MO_xF_y films with respect to various deposition conditions. The XPS depth profiling investigations revealed a uniform distribution of metal, O, and F in the MO_xF_y films. Compositional tunability in MO_xF_y ALD throughout the range from HfO_2 to HfF_4 and ZrO_2 to ZrF_4 was confirmed by both XPS and RBS analyses. The physical sputtering rates of the films were also estimated from the XPS depth-profile measurements. The sputtering rates of pure metal oxides were found to be significantly lower than their metal fluoride counterparts under Ar^+ ion bombardment at 3 keV. The physical sputtering rates increased with fluorine concentration for all MO_xF_y films.

The molar volume expansion for the fluorination of HfO_2 to HfF_4 and the fluorination of ZrO_2 to ZrF_4 is fairly low. The expansion of HfO_2 to HfF_4 and ZrO_2 to ZrF_4 have molar volume ratios of $HfO_2/HfF_4 = 1.66$ and $ZrO_2/ZrF_4 = 1.74$, respectively. These low expansion ratios will generate small strains of $\varepsilon = \Delta l/l = 0.18$ and 0.20 for the Hf and Zr systems, respectively. These smaller strains will minimize the possibility of film cracking and particle generation. As a result of these low expansion ratios and strains, HfO_xF_y and ZrO_xF_y oxyfluoride films should be able to serve as effective protective coatings in fluorine and oxygen-containing plasma environments.

ACKNOWLEDGMENT

The authors thank Ryan Thorpe from the Laboratory for Surface Modification at Rutgers University for the RBS measurements.

DATA AVAILABILITY

The data that support the findings of this study are available within the article.

REFERENCES

[1]A. Agarwal and M. J. Kushner, J. Vac. Sci. Technol. A **26**, 498 (2008).
[2]N. Ito, T. Moriya, F. Uesugi, M. Matsumoto, S. Liu, and Y. Kitayama, Jpn. J. Appl. Phys. **47**, 3630 (2008).
[3]H. Shih, "A systematic study and characterization of advanced corrosion resistance materials and their applications for plasma etching processes in semiconductor silicon wafer fabrication," in *Corrosion Resistance*, edited by H. Shih (InTech, 2012), ISBN: 978-953-5-0467-4, see http://www.intechopen.com/books/corrosion-resistance/
[4]M. J. Sowa, J. Vac. Sci. Technol. A **32**, 01A106 (2014).
[5]S. Xu, Z. Sun, X. Qian, J. Holland, and D. Podlesnik, J. Vac. Sci. Technol. B **19**, 166 (2001).
[6]D.-M. Kim, M.-R. Jang, Y.-S. Oh, S. Kim, S.-M. Lee, and S.-H. Lee, Surf. Coat. Technol. **309**, 694 (2017).
[7]K. Miyashita, T. Tsunoura, K. Yoshida, T. Yano, and Y. Kishi, Jpn. J. Appl. Phys. **58**, SEEC01 (2019).
[8]T.-K. Lin, W.-K. Wang, S.-Y. Huang, C.-T. Tasi, and D.-S. Wuu, Nanomaterials **7**, 183 (2017).
[9]K. Miwa, N. Takada, and K. Sasaki, J. Vac. Sci. Technol. A **27**, 831 (2009).
[10]D.-M. Kim, Y.-S. Oh, S. Kim, H.-T. Kim, D.-S. Lim, and S.-M. Lee, Thin Solid Films **519**, 6698 (2011).
[11]J.-B. Song, J.-T. Kim, S.-G. Oh, and J.-Y. Yun, Coatings **9**, 102 (2019).
[12]T. Goto, Y. Shiba, A. Teramoto, Y. Kishi, and S. Sugawa, J. Vac. Sci. Technol. A **38**, 043003 (2020).
[13]N. Mahuli, A. S. Cavanagh, and S. M. George, J. Vac. Sci. Technol. A **38**, 022407 (2020).
[14]Y. Shiba, A. Teramoto, T. Goto, Y. Kishi, Y. Shirai, and S. Sugawa, J. Vac. Sci. Technol. A **35**, 021405 (2017).
[15]R. Tahara, T. Tsunoura, K. Yoshida, T. Yano, and Y. Kishi, Jpn. J. Appl. Phys. **57**, 06JF04 (2018).
[16]T. Tsunoura, K. Yoshida, T. Yano, and Y. Kishi, Jpn. J. Appl. Phys. **56**, 06HC02 (2017).
[17]J. Y. S. Sun, X.-M., He, and S. Thach, Plasma Resistant Coatings for Plasma Chamber Components (Applied Materials, Inc., Santa Clara, CA, 2012).
[18]S. Fujihara, T. Kato, and T. Kimura, J. Mater. Sci. Lett. **20**, 687 (2001).
[19]S. J. Jiang, Z. C. Jin, and C. G. Granqvist, Appl. Opt. **27**, 2847 (1988).
[20]Y. Y. Yu, D. S. Kim, and K. Char, J. Appl. Phys. **96**, 6393 (2004).
[21]W.-K. Wang, Y.-X. Lin, and Y.-J. Xu, Nanomaterials **8**, 936 (2018).
[22]S. Y. Zheng, A. M. Andersson-Fäldt, B. Stjerna, and C. G. Granqvist, Appl. Opt. **32**, 6303 (1993).
[23]T.-K. Lin, D.-S. Wuu, S.-Y. Huang, and W.-K. Wang, Coatings **8**, 373 (2018).
[24]G. Malandrino, L. M. S. Perdicaro, and I. L. Fragalà, Chem. Vap. Deposition **12**, 736 (2006).
[25]V. Cremers, R. L. Puurunen, and J. Dendooven, Appl. Phys. Rev. **6**, 021302 (2019).
[26]J. W. Elam, D. Routkevitch, P. P. Mardilovich, and S. M. George, Chem. Mater. **15**, 3507 (2003).
[27]S. M. George, Chem. Rev. **110**, 111 (2010).
[28]A. I. Abdulagatov, Y. Yan, J. R. Cooper, Y. Zhang, Z. M. Gibbs, A. S. Cavanagh, R. G. Yang, Y. C. Lee, and S. M. George, ACS Appl. Mater. Interfaces **3**, 4593 (2011).
[29]J. S. Daubert, G. T. Hill, H. N. Gotsch, A. P. Gremaud, J. S. Ovental, P. S. Williams, C. J. Oldham, and G. N. Parsons, ACS Appl. Mater. Interfaces **9**, 4192 (2017).
[30]S. Mirhashemihaghighi, J. Swiatowska, V. Maurice, A. Seyeux, S. Zanna, E. Salmi, M. Ritala, and P. Marcus, Corros. Sci. **106**, 16 (2016).
[31]S. E. Potts *et al.*, J. Electrochem. Soc. **158**, C132 (2011).
[32]B. Diaz, E. Harkonen, J. Swiatowska, V. Maurice, A. Seyeux, P. Marcus, and M. Ritala, Corros. Sci. **53**, 2168 (2011).
[33]E. Marin, L. Guzman, A. Lanzutti, W. Ensinger, and L. Fedrizzi, Thin Solid Films **522**, 283 (2012).
[34]C. X. Shan, X. H. Hou, and K. L. Choy, Surf. Coat. Technol. **202**, 2399 (2008).

[35]R. Cooper, H. P. Upadhyaya, T. K. Minton, M. R. Berman, X. H. Du, and S. M. George, Thin Solid Films **516**, 4036 (2008).
[36]T. K. Minton, B. H. Wu, J. M. Zhang, N. F. Lindholm, A. I. Abdulagatov, J. O'Patchen, S. M. George, and M. D. Groner, ACS Appl. Mater. Interfaces **2**, 2515 (2010).
[37]V. Miikkulainen, M. Leskelä, M. Ritala, and R. L. Puurunen, J. Appl. Phys. **113**, 021301 (2013).
[38]D. M. Hausmann, E. Kim, J. Becker, and R. G. Gordon, Chem. Mater. **14**, 4350 (2002).
[39]K. Kukli, M. Ritala, T. Sajavaara, J. Keinonen, and M. Leskelä, Chem. Vap. Deposition **8**, 199 (2002).
[40]J. Niinistö, M. Putkonen, L. Niinistö, F. Song, P. Williams, P. N. Heys, and R. Odedra, Chem. Mater. **19**, 3319 (2007).
[41]M. Ritala, M. Leskela, L. Niinisto, T. Prohaska, G. Friedbacher, and M. Grasserbauer, Thin Solid Films **250**, 72 (1994).
[42]K. Kukli, T. Pilvi, M. Ritala, T. Sajavaara, J. Lu, and M. Leskelä, Thin Solid Films **491**, 328 (2005).
[43]M. Cho, H. B. Park, J. Park, S. W. Lee, C. S. Hwang, G. H. Jang, and J. Jeong, Appl. Phys. Lett. **83**, 5503 (2003).
[44]Y. Lee, H. Sun, M. J. Young, and S. M. George, Chem. Mater. **28**, 2022 (2016).
[45]B. Lee *et al.*, Microelectron. Eng. **86**, 272 (2009).
[46]M. Putkonen, J. Niinistö, K. Kukli, T. Sajavaara, M. Karppinen, H. Yamauchi, and L. Niinistö, Chem. Vap. Deposition **9**, 207 (2003).
[47]M. Ritala and M. Leskelä, Appl. Surf. Sci. **75**, 333 (1994).
[48]J. W. Elam, M. D. Groner, and S. M. George, Rev. Sci. Instrum. **73**, 2981 (2002).
[49]*HSC Chemistry 9.1* (Outokumpu Research Oy, Pori).
[50]O. S. Monnahela, B. M. Vilakazi, J. B. Wagener, A. Roodt, P. A. B. Carstens, and W. L. Retief, J. Fluorine Chem. **135**, 246 (2012).
[51]M. P. Seah and T. S. Nunney, J. Phys. D Appl. Phys. **43**, 253001 (2010).
[52]*CRC Handbook of Chemistry and Physics*, 84th ed., edited by D. R. Lide (CRC, Boca Raton, FL, 2003).